A Finite Element Approach for Simplified 2D Nonlinear Dynamic Contact/Impact Analysis

Seungwook Seok[1], Adnan Shahriar[2], Arturo Montoya[2] and Ramesh B. Malla[3*]

[1]Architectural Engineering, Hanyang University, 222 Wangsimni-ro, Seongdong-gu, Seoul, 04763, South Korea (Formerly, Department of Civil and Environmental Engineering, University of Connecticut, Storrs, Connecticut, United States).

[2]Department of Mechanical Engineering, University of Texas at San Antonio, One UTSA Circle, San Antonio, Texas, 78249, United States.

[3*]Department of Civil and Environmental Engineering, University of Connecticut, 261 Glenbrook Road, Storrs, Connecticut, 06269, United States.

*Corresponding author(s). E-mail(s): ramesh.malla@uconn.edu; Contributing authors: sseok@hanyang.ac.kr; adnan.shahriar@utsa.edu; arturo.montoya@utsa.edu;

Abstract

In this paper, a simplified numerical approach for finite element dynamic analysis of an inelastic solid structure subjected to solid object impact is presented. The approach approximates the impacting solid as the selected multiple nodes, for which mass of the impactor is distributed. The node-to-segment contact formulation with the penalty constraint technique incorporated is employed to impose contact conditions between the nodes and the surface of the receiver structure. The node-to-segment algorithm is integrated into Newton-Raphson time integration scheme and the Lagrange multiplier technique is applied to enforce the identical displacements for the selected nodes throughout the analysis process. The approach is verified using two-dimensional plane strain models considering elastic-perfectly-plastic material behavior. The results obtained using the proposed approach are in a good agreement with those simulated using a commercial finite element code, ABAQUS Dynamic/Implicit, in terms of displacements and stress distribution fields. The proposed approach is shown to be computationally superior to general finite element method-based contact/impact analysis without significantly sacrificing the accuracy.

Keywords: Impact, Contact, Node-to-segment, Newton-Raphson method, Lagrange multiplier, Elastic-plastic material

1 Introduction

Finite element method (FEM) is widely used to perform analysis of contact/impact problems in solids (Laursen, 2013). Accurate simulations of contact problems require accurate calculation of contact resistance between two contacting/colliding solids discretized in finite elements (see Fig. 1a). The contact discretization and tracking method that seek for numerical solution to resistance at the contact interface can be classified into three groups: (i) node-to-node (NTN) contact formulation (ii) node-to-segment (NTS) contact formulation and (iii) segment-to-segment (STS) contact formulation (Neto et al, 2016). NTN formulation establishes the contact interaction between the two pair nodes defined at the pre-processing stage. Despite having the simplest formulation among the three methods, this approach has a drawback of not being able to capture large deformations, as the initial pair of the nodes may change under such large deflections (Francavilla and Zienkiewicz, 1975; Stadter and Weiss, 1979). NTS formulation defines a *slave* node on one side of the contact interface and a *master* surface on the opposite side. At the contact interface, *slave* node interacts with a point of projection on the *master* surface (Wriggers et al, 1990; Zavarise and De Lorenzis, 2009b). In this formulation, several *slave* nodes are needed to represent the surface geometry, located at the opposite to the *master* surface. Finally, STS formulation is the most elaborated formulation, in which the contact constraint is imposed in an average sense over regions of the *master* and *slave* surfaces (Puso and Laursen, 2004). The main feature of this technique is that it enforces the contact conditions in the weak form integration, not directly in nodal points as done in the other two methods (i.e., NTN and NTS). Typically, STS formulation provides more accurate simulation than NTS formulation (Zavarise and De Lorenzis, 2009a).

Besides the contact formulations, material nonlinearity augments the complexities to the contact/impact problems. Many research work has investigated responses associated with the deformations, and contact stresses and pressures resulting from nonlinear material properties (Jackson and Green, 2005; Ghaednia et al, 2016, 2017). Because of wide variations in nonlinear material constitutive behaviors, most of studies have only focused on the responses with idealized elastic-plastic material models, serving as the basis for understanding the contact characteristics in problems of colliding/contacting solids. Typically, 2D finite element (FE) model, in which, deformable 2D flat surface is in contact with (deformable or rigid) circle, was used to study the effects of the parameters, including geometry, boundary conditions, and material properties, on the contact stress (force), contact area, and initiation of plastic deformation. A simple yield criterion, such as von Mises criterion, was adopted to define the onset of plastic deformation. In some cases, experimental data supported

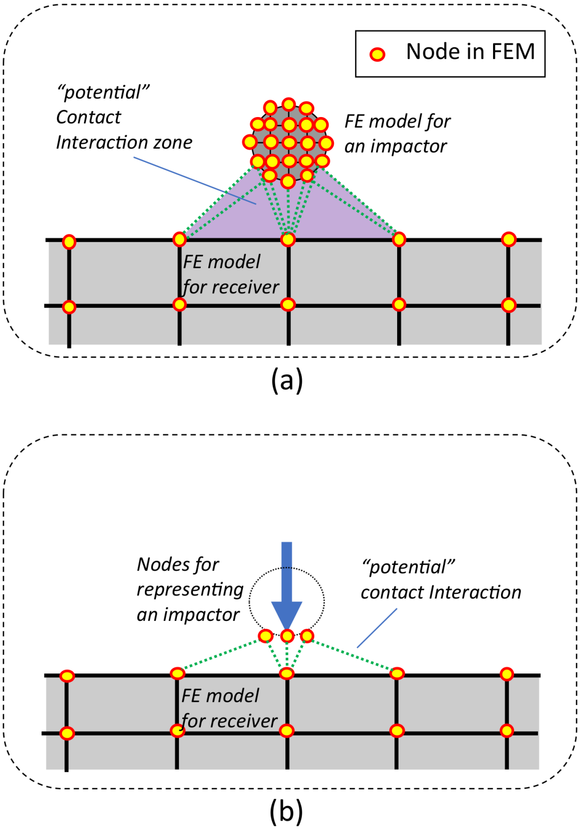

Fig. 1. Schematic description of (a) typical FEM-based contact/impact analysis approach (b) proposed contact/impact analysis approach

the findings from finite element analysis (FEA). Result from the aforementioned numerical and experimental studies were often formulated in analytical expressions for ease of use (Brake, 2012; Alves et al, 2015; Big-Alabo et al, 2015). However, many of these analytical models are limited to "quasi-static" contact mechanisms. In addition, impact problems (or dynamic transient contact problems) are problem-oriented due to their various forms of material nonlinearities and irregular geometric shapes as well as a wide range of impacting velocity, mass, and the associated inertia effects. As such, many impact problems were individually analyzed by means of FEM (Her and Liang, 2004; Zhang et al, 2006; Kumar and Shukla, 2012; Sha and Hao, 2012).

Typically, refined mesh in the vicinity of the contact/impact zone is inevitable to simulate the progressive structural/material response over problem evolution. Accuracy of FEA result is closely dependent on the mesh quality. In some cases, such as hail impact or drop weight impact on structures, the impact object is very small when compared to the entire volume of a receiver structure, while it impacts with high enough inertia (e.g., mass and speed) to create damage within the localized zone of a structure. As a result, creating finer FE mesh in accordance with small impacting object all over the receiver structure could be computationally expensive. This study was motivated by such cases to deal with the problems in a computationally efficient way.

The present study aims at suggesting a numerical scheme for FE dynamic analysis of an inelastic solid structure subjected to "small" solid object impact. A 2D NTS-based approach for formulating an impact problem is proposed, in which FE modeling and meshing for the body of the impacting object is not required, unlike the traditional FEM-based contact/impact analysis (Fig. 1a). Instead, the body of the impactor is represented with one or more selected node(s) (Fig. 1b) and the mass of the impactor is applied to the considered node(s) in a distributed fashion based on the geometry of the impact body. The implicit time integration scheme, Newton-Raphson method, is chosen for solving the equation of motion for the impact problem. The proposed approach is verified by applying the method to 2D plane strain example models and comparing with the corresponding results simulated with a commercial FEA software, ABAQUS Dynamic/Implicit.

2 Methodology

2.1 Modeling Assumptions

Finite element contact/impact analysis requires refined mesh resolution for both an impactor and a receiver in the vicinity of the contact/impact zone to provide accurate results. This refined analysis is particularly needed when failure stresses and deformations of the receiver structure is of the interest to investigate. When the impactor is tiny relative to the volume of the receiver, say less than 1% of the receiver, a generally accepted modeling strategy is not to physically model the impactor and instead to assume it as a concentrated point load. Such an approximation method can cause less accurate and inconsistent responses.

A computationally efficient and robust FE formulation is suggested, effective to the following impact problem cases: (i) the impacting body is sufficiently "small" compared to the receiver structure, and (ii) the impact event causes only a localized structural defect (i.e., localized material plasticity). For the numerical scheme to be proposed, two prerequisite assumptions are made: (i) the size of the impact object is smaller than that of one finite element size in the receiver structure, as shown in Fig. 1, and (ii) the impactor is assumed to be rigid.

2.2 Enforcement of Contact Constraints Using NTS Algorithm

The governing assumption is that the physical body of an impacting solid object can be approximated by nodal point load. As such, to deal with the contact condition between the nodal point load and the surface of the receiver structure (see Fig. 2a), a well-known NTS contact algorithm is adopted, as it has shown its ability to properly simulate the actual contact mechanism in many engineering applications (Khoei et al, 2013; Lee et al, 2016; Xing et al, 2019). For detailed information about the NTS algorithm, see the work of Zavarise and De Lorenzis (2009b). Within the context of

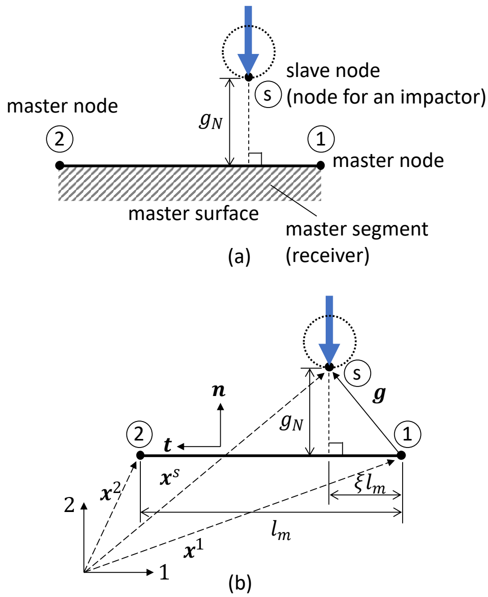

Fig. 2. NTS contact approach: (a) contact geometry of a receiver element in contact with an impactor node s (b) geometrical meanings of various scalar and vector variables defined in the NTS geometry.

NTS contact algorithm, enforcement of contact constraint between the contact surface and the impactor node is typically carried out using the penalty method (Zavarise and De Lorenzis, 2009b).

A schematic view of the NTS geometry is presented in Fig. 2b, in which the impactor node, s (*slave*), is not perfectly aligned with one of the nodes (1 and 2) in the receiver (*master*) surface in the normal direction. The normal distance between the impactor (*slave*) node and the receiver (*master*) surface is called "gap", g_N, and is given by: (Zavarise and De Lorenzis, 2009b)

$$g_N = \boldsymbol{g} \cdot \boldsymbol{n} = (\boldsymbol{x}^s - \boldsymbol{x}^1) \cdot \boldsymbol{n} \tag{1}$$

where $\boldsymbol{n}$ is the normal unit vector orthogonal to the *master* surface, $\boldsymbol{x}^s$ and $\boldsymbol{x}^1$ are the vectors identifying the current positions, respectively, of nodes s and 1, and $\boldsymbol{g}$ is the distance vector between the nodes s and 1.

As intuitively expected from Fig. 2, the contact between the impactor and receiver is physically initiates when $g_N = 0$ and it remains in active only if $g_N \leq 0$ (i.e., when indentation exists). Following the penalty method, the contact contribution to the potential Φ^{con} is defined as: (Zavarise and De Lorenzis, 2009b)

$$\Phi^{con} = \frac{1}{2}\epsilon_N g_N^2 \tag{2}$$

where ϵ_N is the penalty parameter. The choice of penalty parameter, ϵ_N, should be made carefully, as it can influence the contact-induced duration, force, and indentation (degree of penetration). Following the sensitivity analysis (see Appendix A for details), this study used the value of ϵ_N to be equal to the modulus of elasticity of the receiver.

The matrix-form of the nonlinear equation of motion represented by the FE discretization of the receiver coupled with the discretized contact area can be written as: (Suwannachit et al, 2012)

$$\boldsymbol{M}\ddot{\boldsymbol{u}} + \boldsymbol{C}\dot{\boldsymbol{u}} + \boldsymbol{f}^{int} + \boldsymbol{f}^{con} = \boldsymbol{f}^{ext} \tag{3}$$

where $\boldsymbol{M}$ is the mass matrix and $\boldsymbol{C}$ is the damping matrix. $\boldsymbol{u}$ is the displacement vector, with the overdot $(\cdot)$ denoting the time derivative. $\boldsymbol{f}$ represents the nodal force vector. The superscripts int, con, and ext on $\boldsymbol{f}$ are the abbreviations for internal, contact, and external forces.

The residual (or called the out-of-balance) force vector, which will be used for time integration scheme to be presented in the following section, is constructed using the foregoing force vectors such that:

$$\boldsymbol{R} = \boldsymbol{f}^{ext} - \boldsymbol{f}^{int} - \boldsymbol{f}^{con} \tag{4}$$

The mass matrix is constructed as:

$$\boldsymbol{M} = \begin{bmatrix} \boldsymbol{M}^{rec} & \boldsymbol{0} \\ \boldsymbol{0} & \boldsymbol{M}^{imp} \end{bmatrix} \tag{5}$$

where $\boldsymbol{M}^{rec}$ is the mass matrix of a receiver structure only and $\boldsymbol{M}^{imp}$ is the mass matrix or scalar value depending upon the number of nodal points representing the impacting solid.

Similarly, displacement vector $\boldsymbol{u}$ is set up such that:

$$\boldsymbol{u} = \begin{Bmatrix} \boldsymbol{u}^{rec} \\ \boldsymbol{u}^{imp} \end{Bmatrix} \tag{6}$$

where $\boldsymbol{u}^{rec} = \{u_x^1, u_y^1, \ldots, u_x^n, u_y^n\}^T$ is the displacement vector for the receiver structure, in which the subscripts x and y stand for the x-direction and y-direction, respectively, and n is total number of nodes for the receiver structure. $\boldsymbol{u}^{imp} = \{u_x^s, u_y^s\}^T$ is the displacement vector of the impactor, in which the superscript s represents the impactor's node, and as intuitively expected, it follows that in this case, $s = n + 1$.

Solving Eq. 3 using the Newton-Raphson method requires the stiffness matrix given by the exact Jacobian of $\boldsymbol{R}$ for each iteration j (Laursen, 2013). At the current time step $t+\Delta t$ with Δt being the simulation time increment, the nonlinear equation, Eq. 3, is linearized as Eq. 7 presented below.

$$\boldsymbol{M}\,{}^{t+\Delta t}\ddot{\boldsymbol{u}}_j + \boldsymbol{C}\,{}^{t+\Delta t}\dot{\boldsymbol{u}}_j + {}^{t+\Delta t}\boldsymbol{K}_{T_{j-1}}\Delta\boldsymbol{u}_j = {}^{t+\Delta t}\boldsymbol{f}^{ext} - {}^{t+\Delta t}\boldsymbol{f}^{con}_{j-1} - {}^{t+\Delta t}\boldsymbol{f}^{int}_{j-1} \tag{7}$$

where $\boldsymbol{K}_T$ is the algorithmic tangent operator.

Using the time integration scheme to be discussed in the following section, Eq. 7 is iteratively solved within a time step $t + \Delta t$ until the convergence tolerance is satisfied; e.g., the out-of-balance force $\boldsymbol{R}_j^{eff}$ or the displacement increment Δu_j is sufficiently small (Suwannachit et al, 2012; Bathe, 2016).

In Eq. 7, $\boldsymbol{K}_{T_{j-1}}$ is evaluated using the force and state variables of the previous iteration $j-1$, that is,

$$\boldsymbol{K}_{T_{j-1}} = \boldsymbol{K}_{T_{j-1}}^{int} + \boldsymbol{K}_{T_{j-1}}^{con} = \frac{\partial \boldsymbol{f}_{j-1}^{int}}{\partial \boldsymbol{u}_{j-1}} + \frac{\partial \boldsymbol{f}_{j-1}^{con}}{\partial \boldsymbol{u}_{j-1}} \tag{8}$$

with $\boldsymbol{K}_{T_0} = \boldsymbol{K}$, in which $\boldsymbol{K}$ is the initial stiffness matrix, and $\boldsymbol{K}_T^{int}$ and $\boldsymbol{K}_T^{con}$ denote the tangent stiffness matrices contributed by both the impactor and receiver themselves and from the contact interaction, respectively.

For the case of employing a consistent tangent stiffness matrix, it follows that $\boldsymbol{K}_T^{int} = \boldsymbol{K}$ and thus, $\boldsymbol{K}_T^{int}$ can be kept constant throughout the simulation. The contributions of the contact interaction to $\boldsymbol{K}^{con}$ and to $\boldsymbol{f}^{con}$ must be known and can be implicitly defined as follows when the effect of tangential friction is neglected (Zavarise and De Lorenzis, 2009b).

$$\boldsymbol{K}_{T_j}^{con} = \epsilon_N \boldsymbol{N}_S \boldsymbol{N}_S^T - \frac{\epsilon_N g_{N_{j-1}}^2}{l_m^2} \boldsymbol{N}_0 \boldsymbol{N}_0^T \tag{9}$$

and

$$\boldsymbol{f}_{j-1}^{con} = \epsilon_N g_{N_{j-1}} \boldsymbol{N}_S \tag{10}$$

where

$$\boldsymbol{N}_0 = \{\boldsymbol{0}, -\boldsymbol{n}, \boldsymbol{n}\}^T \tag{11}$$

$$\boldsymbol{N}_S = \{-\boldsymbol{n}, -(1-\xi)\boldsymbol{n}, \xi\boldsymbol{n}\}^T \tag{12}$$

In the above equations , $\boldsymbol{n} = \{0, 1\}^T$ and $\boldsymbol{0} = \{0, 0\}^T$. ξ is the tangential projection of g, normalized to the *master* segment length l_m as shown in Fig. 2b. When g_N is sufficiently small to be negligible, Eq. 9 can be simplified by dropping the second term in the right hand side of the equation.

2.3 Time Integration of Nonlinear Equation of Motion Using Newton-Raphson Method

The classical Newton-Raphson method (Cook et al, 2001) is used to solve the nonlinear equation of motion described in the previous section. In this method, the velocity and acceleration at the iteration j within a time step $t + \Delta t$ are approximated by means of Taylor series expansion. According to Newmark method, these approximates become

$$\boldsymbol{u}_j = \boldsymbol{u}_{j-1} + \Delta t \dot{\boldsymbol{u}}_{j-1} + \frac{1}{2}\Delta t^2 \left[2\beta \ddot{\boldsymbol{u}}_j + (1-2\beta)\ddot{\boldsymbol{u}}_{j-1}\right] \tag{13}$$

$$\dot{\boldsymbol{u}}_j = \dot{\boldsymbol{u}}_{j-1} + \Delta t \left[\gamma \ddot{\boldsymbol{u}}_j + (1-\gamma)\ddot{\boldsymbol{u}}_{j-1}\right] \tag{14}$$

with

$$\begin{aligned} {}^{t+\Delta t}\boldsymbol{u}_0 &= {}^{t}\boldsymbol{u} \\ {}^{t+\Delta t}\dot{\boldsymbol{u}}_0 &= {}^{t}\dot{\boldsymbol{u}} \\ {}^{t+\Delta t}\ddot{\boldsymbol{u}}_0 &= {}^{t}\ddot{\boldsymbol{u}} \end{aligned} \tag{15}$$

where β and γ are the numerical factors that control characteristics of the algorithm in terms of numerical accuracy, stability, and damping.

Solving Eq. 14 for $\ddot{\boldsymbol{u}}_j$ and substituting it into Eq. 13, respectively, yield

$$\ddot{\boldsymbol{u}}_j = \frac{1}{\beta \Delta t^2} \left(\Delta \boldsymbol{u}_j - \Delta t \dot{\boldsymbol{u}}_{j-1} \right) - \left(\frac{1}{2\beta} - 1 \right) \ddot{\boldsymbol{u}}_{j-1} \tag{16}$$

$$\dot{\boldsymbol{u}}_j = \frac{1}{\beta \Delta t} \Delta \boldsymbol{u}_j - \left(\frac{\gamma}{\beta} - 1 \right) \dot{\boldsymbol{u}}_{j-1} - \Delta t \left(\frac{\gamma}{2\beta} - 1 \right) \ddot{\boldsymbol{u}}_{j-1} \tag{17}$$

with

$$\Delta \boldsymbol{u}_j = \boldsymbol{u}_j - \boldsymbol{u}_{j-1} \tag{18}$$

in which, $\Delta \boldsymbol{u}_j$ is the increment in the displacements.

Now, after plugging Eq. 16 and Eq. 17 into Eq. 7, bringing the terms with $\Delta \boldsymbol{u}_j$ to the left-hand side and the others to the right-hand side of the equation gives

$$\boldsymbol{K}^{eff}_{j-1} \Delta \boldsymbol{u}_j = \boldsymbol{R}^{eff}_{j-1} \tag{19}$$

where

$$\boldsymbol{K}^{eff}_{j-1} = \frac{1}{\beta \Delta t^2} \boldsymbol{M} + \frac{1}{\beta \Delta t} \boldsymbol{C} + \boldsymbol{K}_{T_{j-1}} \tag{20}$$

$$\boldsymbol{R}^{eff}_{j-1} = \begin{cases} \boldsymbol{f}^{ext} - \boldsymbol{f}^{int}_{j-1} - \boldsymbol{f}^{con}_{j-1} + \boldsymbol{M} \left[\frac{1}{\beta \Delta t} \dot{\boldsymbol{u}}_{j-1} + \left(\frac{1}{2\beta} - 1 \right) \ddot{\boldsymbol{u}}_{j-1} \right] & \\ \quad + \boldsymbol{C} \left[\left(\frac{\gamma}{\beta} - 1 \right) \dot{\boldsymbol{u}}_{j-1} + \Delta t \left(\frac{\gamma}{2\beta} - 1 \right) \ddot{\boldsymbol{u}}_{j-1} \right] & \text{for } j = 1 \\ \boldsymbol{f}^{ext} - \boldsymbol{f}^{int}_{j-1} - \boldsymbol{f}^{con}_{j-1} - \boldsymbol{M} \ddot{\boldsymbol{u}}_{j-1} - \boldsymbol{C} \dot{\boldsymbol{u}}_{j-1} & \text{for } j \geq 2 \end{cases} \tag{21}$$

Once $\boldsymbol{K}^{eff}_{j-1}$ and $\boldsymbol{R}^{eff}_{j-1}$ are computed, the displacement increment $\Delta \boldsymbol{u}_j$ can be obtained using Eq. 19 as given by

$$\Delta \boldsymbol{u}_j = (\boldsymbol{K}^{eff}_{j-1})^{-1} \boldsymbol{R}^{eff}_{j-1} \tag{22}$$

Then, displacement $\boldsymbol{u}_j$ is updated as

$$\boldsymbol{u}_j = \boldsymbol{u}_{j-1} + \Delta \boldsymbol{u}_j \tag{23}$$

Lastly, velocity and acceleration are updated via Eq. 16 and Eq. 17, respectively.

2.4 Multiple Nodes Representation of Impacting Solid

As mentioned earlier, approximating the entire body of the impacting object as a single nodal point and applying its inertia properties (object mass and speed) to this node can lead to significant stress concentration on the localized impact zone of the receiver structure. This is obvious since the nodal point representing the impactor ignores the effect of contact area and the associated resistance. To overcome this limitation, multiple nodes parallel to the contact surface, are used to exert the equivalent inertia force of the impactor in a distributive way to the receiver structure. At the same time, the mass of the impactor is distributed at these selected nodes based on the impactor geometry.

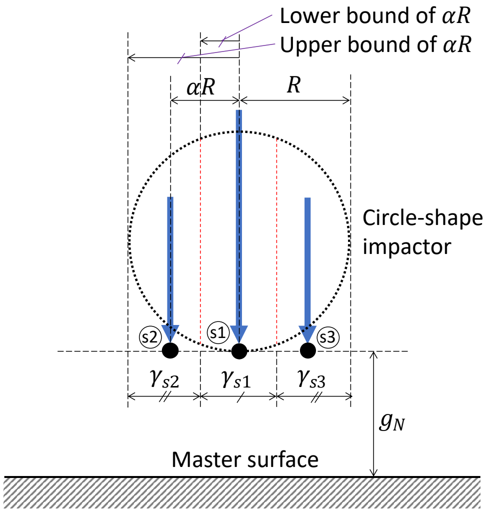

Fig. 3. Nodal points distribution based on the impactor's geometry

As an example, one can consider a circle-shape impactor to be substituted with three nodal points, $s1$ (for center), $s2$ (for left), and $s3$ (for right), positioned in parallel to the contact or receiver surface, as shown in Fig. 3. The impactor body is geometrically sectioned into three vertical parts or sections ($\gamma_{s1} : \gamma_{s2} : \gamma_{s3}$) perpendicular to the contact surface with the width of the left and the right sections being the same (i.e., $\gamma_{s2} = \gamma_{s3}$). The mass distribution ratio for the selected nodes is determined based on the relative area proportion of each part. For example, in the case of $\gamma_{s1} : \gamma_{s2} : \gamma_{s3} = 1 : 1 : 1$, the mass distribution ratio for nodes, $s1$, $s2$, $s3$, becomes about $0.42 : 0.29 : 0.29$. Finally, the position of the left/right nodal point is defined as αR, in which R is the circle radius and α is the ratio factor determining the position. The factor α is bounded by the left/right part of the impactor geometry: the lower bound is the x-direction distance from the center of the impactor to the boundary of the left (or right) node, normalized by R, and the upper bound is the left/right-end distance normalized by R, that is $1.0(= R/R)$. Since the method approximates the physical geometry of the impactor and α is the key parameter that accounts for such approximation, appropriate α has to be determined. This can be done using a trial-and-error approach within the suggested range (upper/lower bounds). However, based on comprehensive analyses as will be seen in Sections 3.1.2 and 3.2, α that gives accurate results is found as about 0.90 for practical impactor geometries, such as circle and square, when $\gamma_{s1} : \gamma_{s2} : \gamma_{s3} = 1 : 1 : 1$. Effect of α on the receiver displacements and stresses will be addressed in those sections.

2.5 Displacement Adjustment Using Lagrange Multiplier Technique

Since the impactor is represented by the selected multiple nodes, these nodes are assumed to have the identical displacements over the impact process. However, applying the NTS algorithm to each of these nodes and solving Eq. 7 by means of the Newton-Raphson iteration scheme does not guarantee that the displacements of all these nodes would be identical throughout the simulation, as they are assigned different distributions of mass depending on different geometrical partitions. Therefore, to impose the identical displacements between those nodes, Lagrange multiplier equation is introduced to the nonlinear time integration scheme described above. This is done following the technique suggested by Leon et al (2012) and it is briefly described below for the particular case considered in this study.

For the impactor represented by three nodes shown in Fig 3, an additional constraint equation for the displacement increment $\Delta \boldsymbol{u}_j$ is given by:

$$\boldsymbol{a}^T \Delta \boldsymbol{u}_j = 0 \tag{24}$$

where

$$\boldsymbol{a} = \{ \underbrace{0, 0, ..., 0, 0}_{\text{corresp. to} \Delta \boldsymbol{u}^{rec}}, \underbrace{0, 2, 0, -1, 0, -1}_{\text{corresp. to} \Delta \boldsymbol{u}^{imp}} \}^T \tag{25}$$

Thus, Eq. 24 yields

$$2 \Delta u_{y_j}^{s1} - \Delta u_{y_j}^{s2} - \Delta u_{y_j}^{s3} = 0 \tag{26}$$

Introducing this constraint condition gives rise to the additional force term in the residual force vector $\boldsymbol{R}^{eff}$, such that Eq. 19 is amended as:

$$\boldsymbol{K}_{j-1}^{eff} \Delta \boldsymbol{u}_j = \overline{\boldsymbol{R}}_{j-1}^{eff} + \Delta \lambda_j \boldsymbol{f}^{ref} \tag{27}$$

in which, λ is the Lagrange (multiplier) parameter, which controls the increment of the reference force vector $\boldsymbol{f}^{ref}$. $\overline{\boldsymbol{R}}_{j-1}^{eff}$ is the “new” residual (out-of-balance) force incorporating the contribution from $\boldsymbol{f}^{ref}$.

The addition of $\Delta \lambda_j \boldsymbol{f}^{ref}$ can be regarded as the addition of external force and it is accumulated throughout the iteration process. It follows that

$$\boldsymbol{f}^{Lag} \leftarrow \boldsymbol{f}^{Lag} + \Delta \lambda_j \boldsymbol{f}^{ref} \tag{28}$$

As such, the effective residual force vector of Eq. 21 is amended such that

$$\overline{\boldsymbol{R}}_{j-1}^{eff} = \boldsymbol{R}_{j-1}^{eff} + \boldsymbol{f}^{Lag} \tag{29}$$

Since the displacement change due to the enforcement of Eq. 26 directly affects the associated contact force, $\boldsymbol{f}^{ref}$ has to be set up using the contact force relation between the receiver and the impactor $\boldsymbol{N}_S$ (Eq. 12), given by:

$$\boldsymbol{f}^{ref} = 2\boldsymbol{N}_S^{s1} - \boldsymbol{N}_S^{s2} - \boldsymbol{N}_S^{s3} \tag{30}$$

where the coefficients for each $\boldsymbol{N}_S$ of the three nodes are determined to be the same as those in Eq. 26.

Combining Eq. 24 and Eq. 27 gives a well-known matrix-form equation incorporated with constraint equation, as follows.

$$\begin{bmatrix} \boldsymbol{K}_{j-1}^{eff} & -\boldsymbol{f}^{ref} \\ \boldsymbol{a}^T & 0 \end{bmatrix} \begin{Bmatrix} \Delta \boldsymbol{u}_j \\ \Delta \lambda_j \end{Bmatrix} = \begin{Bmatrix} \overline{\boldsymbol{R}}_{j-1}^{eff} \\ 0 \end{Bmatrix} \tag{31}$$

To solve this nonsymmetric system of equations, Batoz and Dhatt (1979) presented a technique, which decomposes the iterative displacement vector into two parts.

$$\Delta \boldsymbol{u}_j = \Delta\lambda_j \Delta \boldsymbol{u}_{l_j} + \Delta \boldsymbol{u}_{r_j} \tag{32}$$

where

$$\Delta \boldsymbol{u}_{r_j} = (\boldsymbol{K}^{eff}_{j-1})^{-1} \overline{\boldsymbol{R}}^{eff}_{j-1} \tag{33}$$

$$\Delta \boldsymbol{u}_{l_j} = (\boldsymbol{K}^{eff}_{j-1})^{-1} \boldsymbol{f}^{ref} \tag{34}$$

With some further manipulation, detailed in Leon et al (2012), $\Delta\lambda_j$ is derived as given by.

$$\Delta\lambda_j = \frac{-\boldsymbol{a}^T \Delta \boldsymbol{u}_{r_j}}{\boldsymbol{a}^T \Delta \boldsymbol{u}_{l_j}} \tag{35}$$

with $\Delta\lambda_1 = 0$.

To summarize, for an iteration j at a given time step, $\Delta \boldsymbol{u}_{r_j}$ and $\Delta \boldsymbol{u}_{l_j}$ in Eq. 33 and Eq. 34 are computed. Then, $\Delta\lambda_j$ is computed via Eq. 35. Finally, the displacement increment with the Lagrange constraint condition imposed is obtained by means of Eq. 32.

2.6 NTS-Based Multi-Nodes Contact/Impact Newton-Raphson Scheme

Up to now, it has been discussed how the NTS method, Newton-Raphson method, and Lagrange method are coupled among each other to solve the contact/impact problems considered. The integrated solution scheme is illustrated step-by-step in the flow chart in Fig. 4. The scheme describes the iterative procedure for solving the so-called nonlinear NTS-based multi-nodes contact/impact Newton-Raphson scheme at a given time step only. Finally, the scheme is repeated for each time step, as the simulation time increases.

3 Verification

Two-dimensional plane strain models were used to test the verification of the proposed approach for dynamic analysis of impact problems. An in-house FEA code was written in MATLAB language (MATLAB, 2020) to implement the NTS-based multi-nodes contact/impact Newton-Raphson scheme discussed earlier. The verification of the proposed modeling approach was done by comparison with the commercial FEA software code, ABAQUS (Dassault Systèmes, 2014). In the following sections, the proposed approach will be applied to each of the two different impact problem cases: (i) indentation model, in which a rigid object hits a deformable flat (receiver), and (ii) simply-supported beam model, subjected to transverse impact loading due to rigid object. It should be noted that the indentation model, in which translations at three sides of the receiver structure are restrained (see Fig. 5a), is an idealized model designed to investigate pure elastic-plastic behavior of the structure subjected to rigid impact object, found in many of the published models (Ghaednia et al, 2017). On the

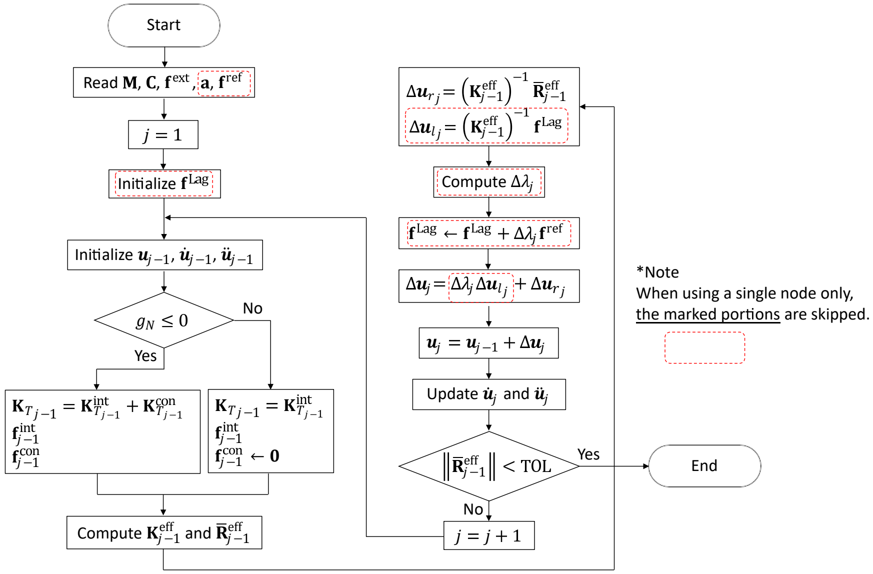

Fig. 4. NTS-based multi-nodes contact/impact Newton-Raphson scheme at a given time step

other hands, the beam model can be regarded as a simple representation for a more realistic behavior of the (receiver) structure that actual overall motion and deflection are accounted for.

3.1 Indentation Model

To build the indetation example shown in Fig. 5, both models (in-house FE model and ABAQUS FE model) used the 8-nodes (quadratic) elements (Q8 elements) with the mesh size of $0.05m$ for the receiver, consisting of a total number of 400 elements. The boundary conditions were modeled such that all sides of the flat structure except the impact side were constrained in the x and y directions (i.e., pinned support). The deformable flat receiver was modeled with an J2 isotropic hardening elastic-perfectly-plastic material model. The following material properties were assumed: $E = 200GPa$, $\rho = 7700kg/m^3$, $\mu = 0.3$, and $\sigma_y = 350MPa$, in which E, ρ, μ, and σ_y are, respectively, Elastic modulus, mass density, Poison's ratio, and yield strength. No damping was applied to the model. The circle-shape impactor body with its radius of $0.025m$ was considered, whose mass and initial velocity was assumed as $0.5kg$ and $500m/s$, respectively. The velocity of $500m/s$ was chosen as the applied velocity of the impactor, as it is high enough to generate the material plastic behavior. In the ABAQUS model, the Dynamic/Implicit solver with the Newton-Raphson method adopted was chosen as the solution solver. The impactor was geometrically modeled and were meshed with Q8 elements with the mesh size of $0.01m$ (Fig. 5b), and the surface-to-surface contact formulation (identical to STS formulation discussed

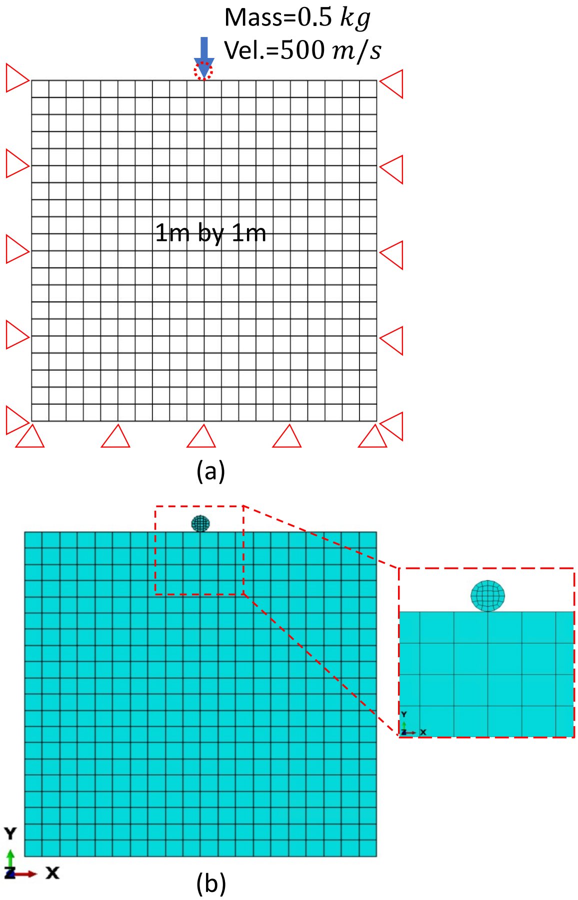

Fig. 5. FE mesh of indentation model and its boundary conditions: (a) In-house FE model, in which the impactor is represented by node(s) (b) ABAQUS model, in which the impactor is modeled using finite element mesh

earlier) was applied at the potential contact interface to account for the contact interaction between the discretized mesh of the receiver and impactor. The rigid body was applied to the impactor of the ABAQUS model. For all the analyses, the simulation time increment was set as 10^{-6} s.

3.1.1 Analysis Using Single Node Representation of Impacting Solid

The first numerical analysis was performed using the proposed approach with a single nodal point impactor and the ABAQUS FEA software. As shown in Fig. 6, the comparison of the results from the two analyses shows that the computed impact forces were reasonably in agreement, while the displacement of the node in contact was overpredicted by the approach using a single-node impactor. The discrepancy in the displacement was attributed to the fact that in the proposed approach, the entire

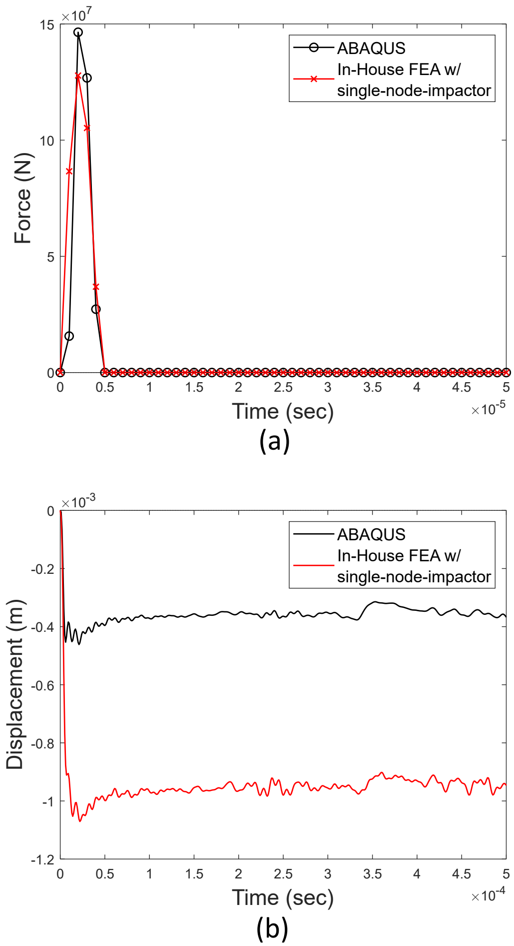

Fig. 6. Comparison of results simulated with ABAQUS subjected to circle-shape impactor and with in-house FEA code subjected to single-node-impactor: (a) Impact force and (b) y-direction (vertical) displacement of the receiver node in impact

impact force was concentrated on the one nodal point in impact, whereas in the ABAQUS, the impact force was exerted on the surface of the receiver in a distributed fashion during the contact interaction.

Fig. 7 presents the von Mises stress (S_{vm}) field distribution developed within the ABAQUS model, at the time of the maximum vertical (i.e., y-dir.) displacement of the center node at the top surface occurring. The corresponding stress distribution fields with respect to four stress components, S_{11}, S_{22}, S_{33}, and S_{12}, are shown in Fig. 8. Fig. 7 can be compared with Fig. 9, in which stress distribution field of S_{vm} developed within the in-house FEA code is depicted. It should be noted that the brightness and saturation used in the colorbar schemes of the ABAQUS and the MATLAB are slightly different. As expected, the maximum stress of the in-house FEA model was

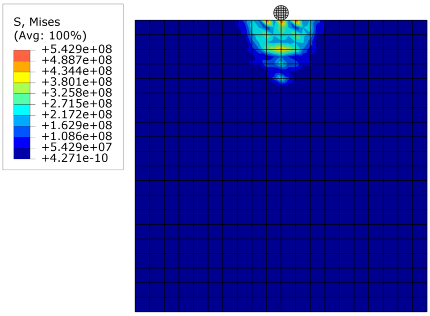

Fig. 7. von Mises stress (S_{vm}) field distribution simulated with ABAQUS

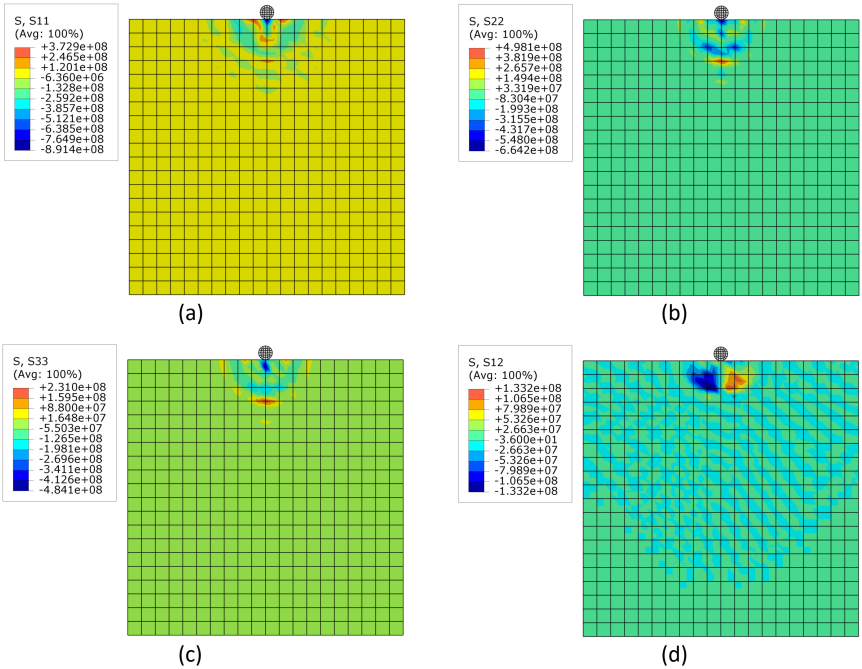

Fig. 8. Stress field distribution simulated with ABAQUS: (a) S_{11} (b) S_{22} (c) S_{33} and (d) S_{12}

higher than that of the ABAQUS model, due to the stress concentration resulting from the single node impact load.

For further investigation, an additional ABAQUS analysis was performed by applying the user-defined impact force-time history, that was obtained from the in-house FEA code for the single-node impact analysis, directly on the receiver without modeling the physical body of impactor with finite element mesh. As shown in Fig. 10b, the results of ABAQUS model and in-house FE model were in a good agreement in terms of the vertical displacement of the node in impact with respect to the

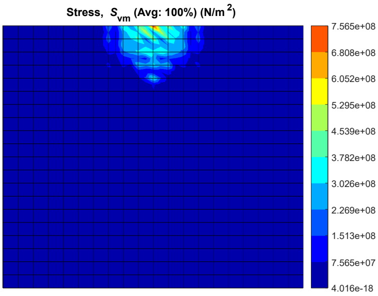

Fig. 9. von Mises stress (S_{vm}) field distribution from in-house FEA code with a single node of impactor

simulation time, when subjected to the identical impact force-time history (see Fig. 10a). This verifies the formulations of the in-house FEA code, giving the confidence of the developed code.

3.1.2 Analysis Using Three Nodes Representation of Impacting Solid

To incorporate the effects of the geometry of the impactor body into the node-based approach, three nodes of impactor were applied to the receiver structure. As described in Section 2.4. The circle-shape impactor depicted in Fig. 3 were partitioned into three parts having the identical widths, $\gamma_{s1} : \gamma_{s2} : \gamma_{s3} = 1 : 1 : 1$, resulting in the mass distribution ratio of $0.42 : 0.29 : 0.29$ for the three nodes. This geometry partition ratio gave rise to α that can range from 0.33 to 1. Thus, the following analyses were carried out using three different α values, i.e., 0.33, 0.9, 1.0. α of 0.33 and α of 1.0 were, respectively, the lower and upper bounds for the given geometry partition. Based on the trial-and-error method, $\alpha = 0.9$ was determined to give a match to the ABAQUS results.

Fig. 11 shows the comparison of the impact force-time history obtained using the ABAQUS and the in-house FEA with the aforementioned three different α values. It was found that the three nodes of impactor approach produced the impact force time profile comparable to ABAQUS analysis, with little effect of α. In Fig. 12b through Fig. 12d, displacement histories with respect to time are presented for the nodes from the top to the bottom shown in Fig. 12a. The comparisons indicate that use of $\alpha = 0.9$ gave a good agreement with ABAQUS analysis results, while slight discrepancy was observed with increasing time and being far away from the impact zone. Overall, considering severe transient dynamic response, such differences seemed reasonable.

As shown in Fig. 13, the von Mises stress field distribution obtained for $\alpha = 0.9$ at the maximum displacement of the first top node presented reasonably accurate results compared with Fig. 7. The stress distribution fields of the four stress components of the plane strain model is depicted in Fig. 14, which showed good consistency with the ABAQUS analysis results presented in Fig. 8.

In order to check whether the ratio parameter $\alpha = 0.9$ found above is also valid for different impactor geometry, an identation model subjected to the square-shape

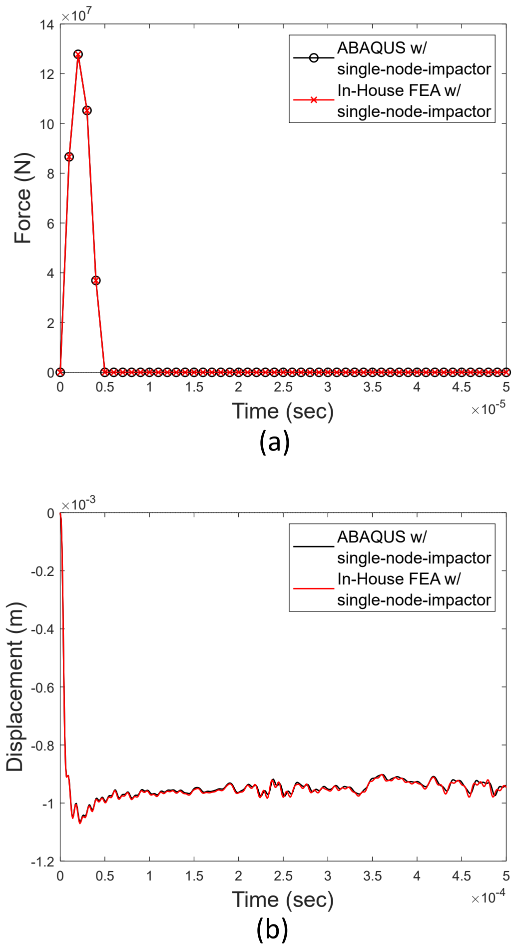

Fig. 10. Comparison of results simulated with ABAQUS and with in-house FEA code (both subjected to single-node-impactor): (a) Impact force and (b) y-direction (vertical) displacement of the receiver node in impact

impactor was built and studied. In the ABAQUS model, the impactor was built as a square-shaped plate with its side $0.0443m$ long, of which dimension was determined to have the same area as its circle-shaped counterpart. In the corresponding in-house FE model, the impactor was again treated as three-nodes and their mass distribution ratio was made as $1:1:1$, assuming the square-shape impactor divided into three equal parts. Effect of α on displacements was studied by taking three values: 0.33, 0.9, 1.0, where 0.33 and 1.0 are the lower and upper bounds, respectively. The results presented in Fig. 15 show that results with $\alpha = 0.9$ are in good agreement with the corresponding ABAQUS results for the nodal displacement histories measured at the same three different positions shown in Fig. 12a. This indicates that there is a no need

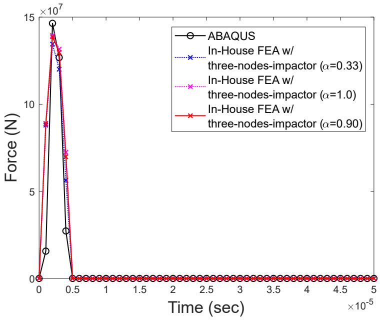

Fig. 11. Impact force simulated with ABAQUS and in-house FEA code considering three nodes representation of impactor, each with different α values, 0.33, 0.9, and 1.0

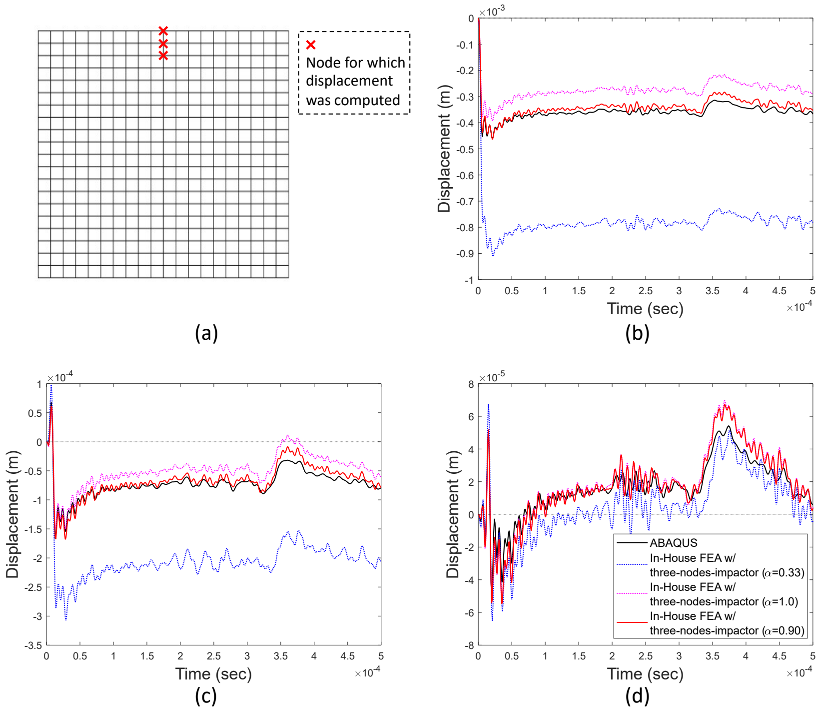

Fig. 12. Comparison of displacements simulated with ABAQUS subjected to circle-shape impactor and with in-house FEA code subjected to three-nodes-impactor: (a) nodes for which displacement were measured (b) vertical displacement of the first node from the top (c) vertical displacement of second node (d) displacement of the third node

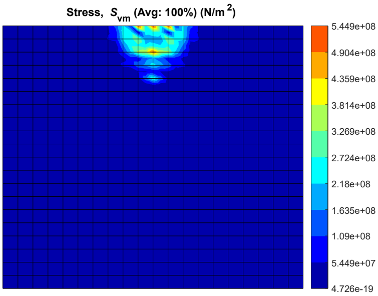

Fig. 13. von Mises stress (S_{vm}) field distribution from in-house FEA code with three nodes representation of impactor and $\alpha = 0.9$

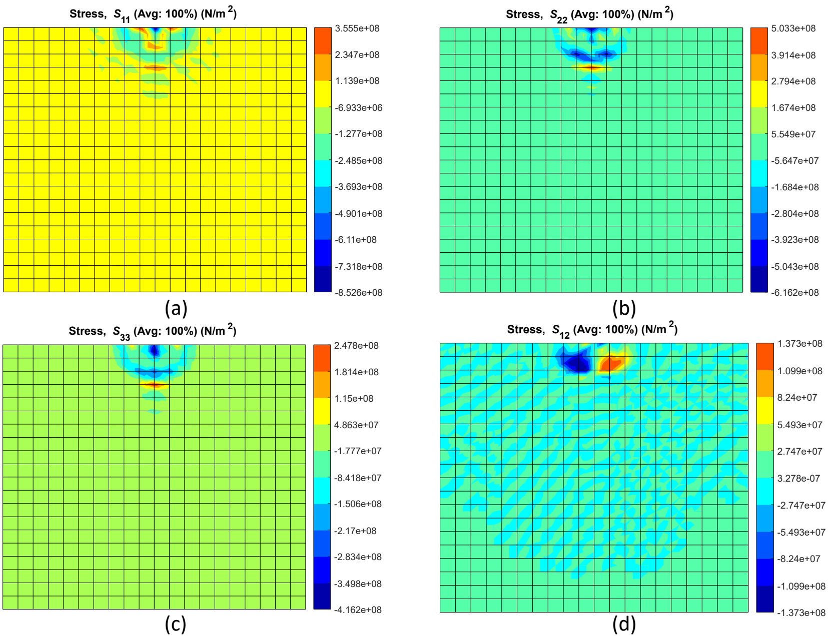

Fig. 14. Stress field distribution from in-house FEA code considering three nodes representation of impactor with $\alpha = 0.9$: (a) S_{11} (b) S_{22} (c) S_{33} and (d) S_{12}

for additional calibration for α and only the redistribution of mass as per the considered impactor geometry is needed when there is a change in impactor geometry. A reason for this is that the impact inertia is applied through the individual masses at the nodal positions considered.

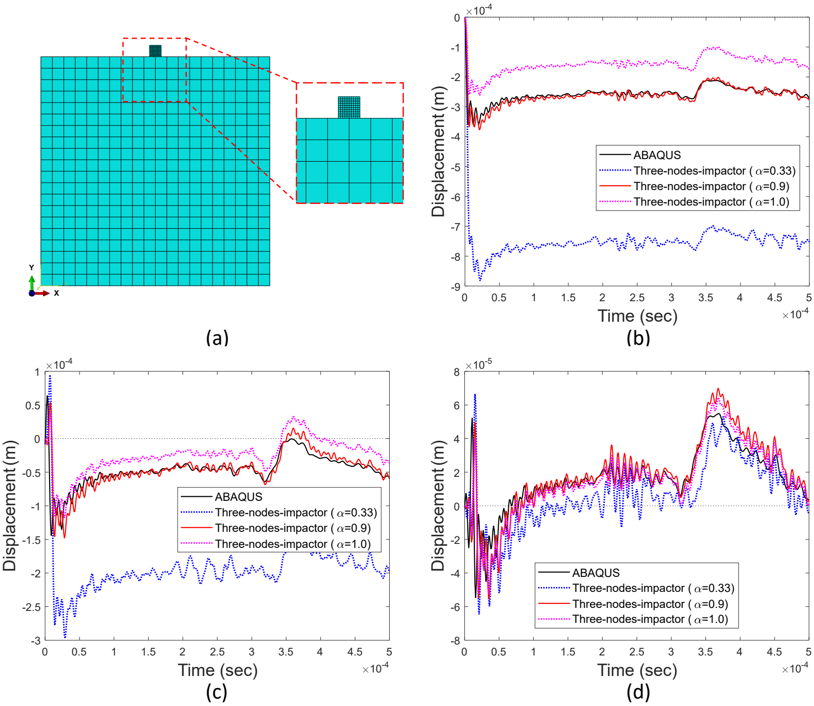

Fig. 15. Comparison of displacements from the ABAQUS model with a square-shape impactor and in-house FEA code with impactor represented by three-nodes: (a) FE mesh (b) vertical displacement of the first node from the top (c) vertical displacement of the second node (d) displacement of the third node (nodes positions presented in Fig. 12a)

3.2 Simply-Supported Beam Model

A simply-supported beam model with $3m$ long and $0.3m$ depth, shown in Fig. 16, was analyzed for additional verification to account for the realistic situation incorporating the deflection of the receiver. As with the previous indentation model, the beam was created using 8-nodes quadratic elements (Q8) with the mesh size of $0.05m$ and J2 elastic-perfectly-plastic material behavior. Material properties and applied mass and velocity were the same as those of indentation model. No damping was considered. To serve as reference, ABAQUS model was created using the aforementioned geometric and material properties in addition to modeling a physical impact object and applying the surface-to-surface formulation (i.e., STS formulation) at the contact interface. Then, an in-house FEA model with the three nodes impact approach was created and was simulated for different α values: 0.3, 0.9, and 1. Note that α of 0.9 was the value found from the above verification example. Fig. 17 compares the analysis results obtained using the ABAQUS and the in-house FEA code. As shown in Fig. 17a, the impact force-time histories computed using in-house FEA code with $\alpha = 0.9$ reasonably matches the force obtained using ABAQUS analysis, similarly

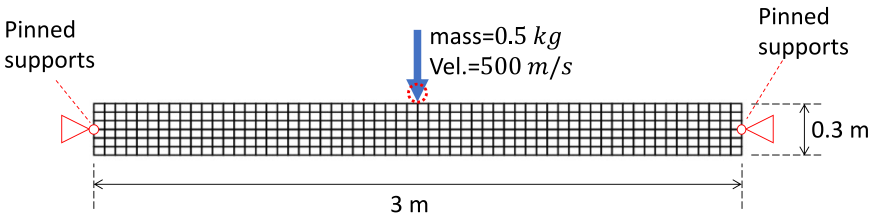

Fig. 16. Finite element mesh of beam model and its boundary conditions, created using in-house FEA code

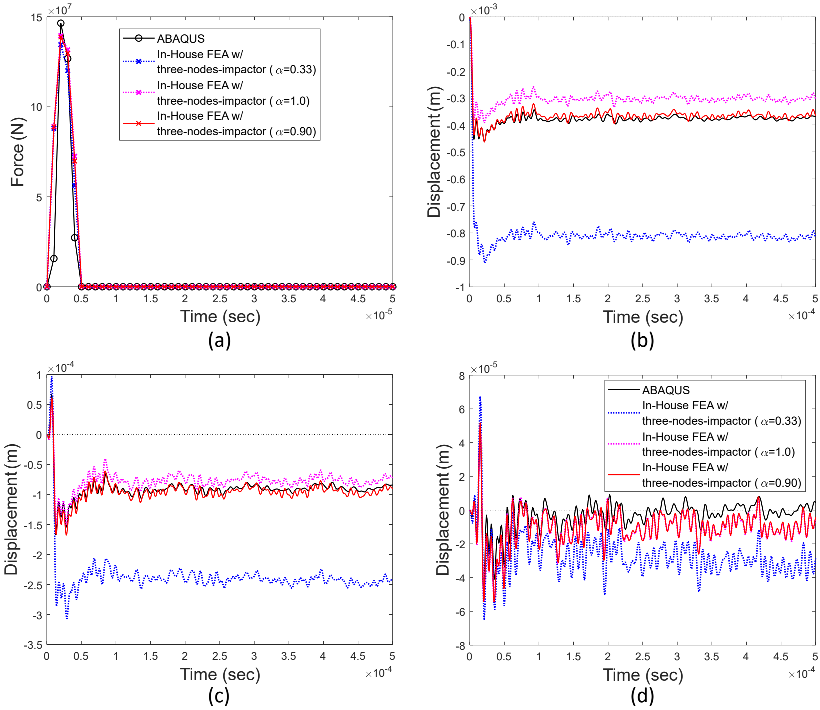

Fig. 17. Comparison of displacements simulated with ABAQUS and in-house FEA code: (a) Impact force (b) vertical displacement of the first node from the top (c) vertical displacement of second node (d) displacement of the third node

to the previous indentation case. Fig. 17b through Fig. 17d show the displacements of the nodes at the midspan, that are, the first, second, and third nodes from the top surface. The comparison results indicate that the displacements obtained using the proposed approach with $\alpha = 0.9$ reasonably agreed with those obtained using ABAQUS analysis. More discrepancies occurred in the third node from the top with increasing time. This is attributed to the accumulation of discrepancies as a node gets far away from the impact location.

3.3 Discussion on the Proposed Approach

In short, although it is simple and straightforward to implement, the presented impact analysis approach achieves an excellent accuracy on the analysis of the impactor hitting a deformable (elastic-perfectly-plastic) body. Based on the presented verification examples with a circle-shaped or square-shaped impact solid, it was found that α value of about 0.9 gave best matching results to the corresponding ABAQUS Dynamic/Implicit analysis results. The presented approach has the advantage of being computationally efficient over classical finite element impact analysis. Furthermore, in the classical approach, creating finer element mesh over a receiver body, as needed owing to the small size of an impacting object, could be not only computationally expensive but also create unforeseen modeling challenges, and thus can take significant time and effort to achieve desirable results. In fact, the computational time between the classical approach and the proposed approach, measured from the indentation model example with a circle-shape impactor, was compared. To run the total simulation time of $0.002\ s$, the proposed approach took $147\ s$, while the classical approach taking $562\ s$; thus, showing the proposed approach almost four times faster.

4 Conclusions

This study presents a simplified finite element approach for the analysis of impact problems, which requires less computational effort than typical finite element contact/impact analysis and is straightforward to implement. The approach approximates the impacting solid as the selected multiple nodes placed in parallel to the contact surface, at which mass of the impactor is distributed in certain proportion according to the sectioned geometry of the impacting solid. The proposed numerical solution scheme is based on Newton-Raphson time integration method that is integrated with the node-to-surface contact algorithm incorporating penalty constraint method and Lagrange multiplier technique, which allows to account for contact interaction between the selected nodes and the surface of the receiver structure. The proposed approach is verified using 2D plane strain models considering elastic-perfectly-plastic material behavior for two specific cases: (i) indentation model and (ii) beam model, each subjected to impacting solid. The simulation results obtained using the approach are in good agreement with ABAQUS Dynamic/Implicit analysis results, e.g., in terms of the impact force, displacements, and stress distribution fields.

In the proposed formulation, the parameter α determines the positions of additional nodes, which are used to approximately represent the contact area resulting from an impact solid. The sensitivity analysis results on varying α values indicated that α has a significant impact on the simulated results. However, for most of the practical purpose, the impactor geometry can be assumed as a circle, oval (with two similar length diameters), or square, and α value of 0.9 is found to be a good estimate that can represent those impactor geometries. When the impactor geometry was changed, for example, from a circle-shape to a square-shape, the only parameter that needs to be adjusted for this change is the mass distribution ratio to the selected nodes, which can be explicitly determined based on the geometrical partition ratio.

The proposed approach is computationally much more superior to the typical finite element contact analysis, without significantly sacrificing the accuracy. This is possible made by omitting physical modeling of the impactor and the associated mesh discretization. In particular, the present approach is expected to be efficient for case where there are multiple impact events to the receiver.

5 Acknowledgments

This work was in part supported by a Space Technology Research Institutes grant (No. 80NSSC19K1076) from the National Aeronautics and Space Administration (NASA)'s Space Technology Research Grants Program. Additionally, the authors are grateful for the continuous support received from the University of Connecticut and its Department of Civil and Environmental Engineering throughout this research.

6 Declarations

Conflicts of interest/Competing interests: The authors declare that they have no conflict of interest. Financial interests: The authors have no relevant financial or non-financial interests to disclose.

Appendix

A Sensitivity Analysis of Penalty Parameter

Many studies (for example, Asano, 1986; Goudreau and Hallquist, 1982; Hallquist et al, 1985; Kulak, 1989; Pham et al, 2018) have been extensively conducted to find the optimum value or range for the penalty parameter (in Eq. 2) that ensures reliable and accurate analysis results. Comparison of the suggested ranges for the penalty parameter in these studies shows the penalty parameter can differ by at most the order of magnitude 10^7 times depending upon the used materials, contact geometries, element types, etc. Unfortunately, no universal analytical expression for determining appropriate penalty parameter value exists. Therefore, this study carried out sensitivity analysis for the choice of penalty stiffness.

The penalty stiffness values were adjusted proportional to the Young's modulus of the receiver material, as $\epsilon_N = \kappa E^{rec}$, where E^{rec} is the Young's modulus of the receiver material and κ is the associated scale factor. A wide range of κ was considered. To this end, κ was set to increase 10 times for each individual run from 10^{-2} to 10^{+2}. The indentation model (Section 3.1.2) was used for this sensitivity test. Fig. A1 shows results of the computed impact force and displacement of the node in impact for different κ values considered. As expected, both the impact force and the local nodal displacement were very sensitive to variation in the penalty parameter. Out of the five simulation runs, the run with $\kappa = 1$ (i.e., $\epsilon_N = E^{rec}$) provided the force and displacement histories the most comparable to the ABAQUS results. It should be mentioned that a more accurate result was obtained with $\kappa = 1.1$ but the difference was not significant when compared with $\kappa = 1$.

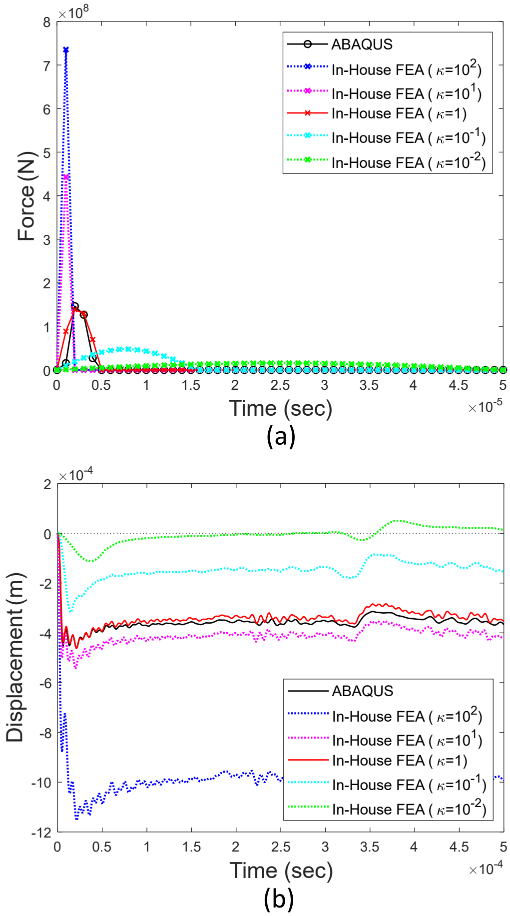

Fig. A1. Sensitivity analysis results of the penalty parameter ϵ_N: (a) Impact force and (b) y-direction (vertical) displacement of the receiver node in impact

References

Alves J, Peixinho N, da Silva MT, et al (2015) A comparative study of the viscoelastic constitutive models for frictionless contact interfaces in solids. Mechanism and Machine Theory 85:172–188. https://doi.org/10.1016/j.mechmachtheory.2014.11.020, URL http://www.sciencedirect.com/science/article/pii/S0094114X14003024

Asano N (1986) A virtual work principle using penalty function method for impact contact problems of two bodies. Bulletin of JSME 29(249):731–736

Bathe KJ (2016) Finite Element Procedures, 2nd edn. Prentice Hall, Prarson Education, Inc., Watertown, MA, USA

Batoz J, Dhatt G (1979) Incremental displacement algorithms for nonlinear problems. International Journal for Numerical Methods in Engineering 14(8):1262–1267

Big-Alabo A, Harrison P, Cartmell MP (2015) Contact model for elastoplastic analysis of half-space indentation by a spherical impactor. Computers & Structures 151:20–29. https://doi.org/10.1016/j.compstruc.2015.01.005, URL http://www.sciencedirect.com/science/article/pii/S0045794915000140

Brake M (2012) An analytical elastic-perfectly plastic contact model. International Journal of Solids and Structures 49(22):3129–3141. https://doi.org/10.1016/j.ijsolstr.2012.06.013, URL http://www.sciencedirect.com/science/article/pii/S0020768312002703

Cook RD, Malkus DS, Plesha ME, et al (2001) Concepts and applications of finite element analysis, 4th edn. Wiley, New York, NY, USA

Dassault Systèmes (2014) ABAQUS 6.14 analysis user's manual. Providence, RI, USA

Francavilla A, Zienkiewicz OC (1975) A note on numerical computation of elastic contact problems. International Journal for Numerical Methods in Engineering 9:913–924. https://doi.org/10.1002/nme.1620090410, URL https://doi.org/10.1002/nme.1620090410

Ghaednia H, Pope SA, Jackson RL, et al (2016) A comprehensive study of the elasto-plastic contact of a sphere and a flat. Tribology International 93:78–90. https://doi.org/10.1016/j.triboint.2015.09.005, URL http://www.sciencedirect.com/science/article/pii/S0301679X15004053

Ghaednia H, Wang X, Saha S, et al (2017) A Review of Elastic–Plastic Contact Mechanics. Applied Mechanics Reviews 69(060804). https://doi.org/10.1115/1.4038187, URL https://doi.org/10.1115/1.4038187

Goudreau G, Hallquist J (1982) Recent developments in large-scale finite element lagrangian hydrocode technology. Computer Methods in Applied Mechanics and Engineering 33(1):725–757. https://doi.org/10.1016/0045-7825(82)90129-3, URL https://www.sciencedirect.com/science/article/pii/0045782582901293

Hallquist J, Goudreau G, Benson D (1985) Sliding interfaces with contact-impact in large-scale Lagrangian computations. Computer Methods in Applied Mechanics and Engineering 51(1):107–137. https://doi.org/10.1016/0045-7825(85)90030-1, URL https://www.sciencedirect.com/science/article/pii/0045782585900301

Her SC, Liang YC (2004) The finite element analysis of composite laminates and shell structures subjected to low velocity impact. Composite Structures 66(1-4):277–285

Jackson RL, Green I (2005) A Finite Element Study of Elasto-Plastic Hemispherical Contact Against a Rigid Flat. Journal of Tribology 127(2):343–354. https://doi.org/10.1115/1.1866166, URL https://doi.org/10.1115/1.1866166

Khoei A, Biabanaki S, Parvaneh S (2013) 3D dynamic modeling of powder forming processes via a simple and efficient node-to-surface contact algorithm. Applied Mathematical Modelling 37(1):443–462. https://doi.org/10.1016/j.apm.2012.03.010, URL http://www.sciencedirect.com/science/article/pii/S0307904X12001485

Kulak R (1989) Adaptive contact elements for three-dimensional explicit transient analysis. Computer Methods in Applied Mechanics and Engineering 72(2):125–151. https://doi.org/10.1016/0045-7825(89)90156-4, URL https://www.sciencedirect.com/science/article/pii/0045782589901564

Kumar N, Shukla M (2012) Finite element analysis of multi-particle impact on erosion in abrasive water jet machining of titanium alloy. Journal of Computational and Applied Mathematics 236(18):4600–4610

Laursen TA (2013) Computational contact and impact mechanics: fundamentals of modeling interfacial phenomena in nonlinear finite element analysis. Springer Science & Business Media

Lee J, Liu W, Hong JW (2016) Impact fracture analysis enhanced by contact of peridynamic and finite element formulations. SI: Experimental Testing and Computational Modeling of Dynamic Fracture 87:108–119. https://doi.org/10.1016/j.ijimpeng.2015.06.012, URL http://www.sciencedirect.com/science/article/pii/S0734743X15001281

Leon SE, Paulino GH, Pereira A, et al (2012) A Unified Library of Nonlinear Solution Schemes. Applied Mechanics Reviews 64(4):040,803–040,803–26. https://doi.org/10.1115/1.4006992, URL http://dx.doi.org/10.1115/1.4006992

MATLAB (2020) version 9.8.0 (R2020a). The Mathworks, Inc., Natick, MA, USA

Neto AG, Pimenta PM, Wriggers P (2016) A master-surface to master-surface formulation for beam to beam contact. Part I: frictionless interaction. Computer Methods in Applied Mechanics and Engineering 303:400–429. https://doi.org/10.1016/j.cma.2016.02.005, URL http://www.sciencedirect.com/science/article/pii/S0045782516300275

Pham TM, Hao Y, Hao H (2018) Sensitivity of impact behaviour of RC beams to contact stiffness. International Journal of Impact Engineering 112:155–164. https://doi.org/10.1016/j.ijimpeng.2017.09.015, URL https://www.sciencedirect.com/science/article/pii/S0734743X16310399

Puso MA, Laursen TA (2004) A mortar segment-to-segment contact method for large deformation solid mechanics. Computer methods in applied mechanics and engineering 193(6):601–629

Sha Y, Hao H (2012) Nonlinear finite element analysis of barge collision with a single bridge pier. Engineering Structures 41:63–76. https://doi.org/10.1016/j.engstruct.2012.03.026, URL http://www.sciencedirect.com/science/article/pii/S0141029612001447

Stadter J, Weiss R (1979) Analysis of contact through finite element gaps. Computers & Structures 10(6):867–873. https://doi.org/10.1016/0045-7949(79)90055-5, URL http://www.sciencedirect.com/science/article/pii/0045794979900555

Suwannachit A, Nackenhorst U, Chiarello R (2012) Stabilized numerical solution for transient dynamic contact of inelastic solids on rough surfaces. Computational Mechanics 49(6):769–788. https://doi.org/10.1007/s00466-012-0722-x, URL https://doi.org/10.1007/s00466-012-0722-x

Wriggers P, Vu Van T, Stein E (1990) Finite element formulation of large deformation impact-contact problems with friction. Computers & Structures 37(3):319–331. https://doi.org/10.1016/0045-7949(90)90324-U, URL http://www.sciencedirect.com/science/article/pii/004579499090324U

Xing W, Zhang J, Song C, et al (2019) A node-to-node scheme for three-dimensional contact problems using the scaled boundary finite element method. Computer Methods in Applied Mechanics and Engineering 347:928–956. https://doi.org/10.1016/j.cma.2019.01.015, URL http://www.sciencedirect.com/science/article/pii/S0045782519300209

Zavarise G, De Lorenzis L (2009a) A modified node-to-segment algorithm passing the contact patch test. International Journal for Numerical Methods in Engineering 79(4):379–416. https://doi.org/10.1002/nme.2559, URL https://doi.org/10.1002/nme.2559

Zavarise G, De Lorenzis L (2009b) The node-to-segment algorithm for 2D frictionless contact: Classical formulation and special cases. Computer Methods in Applied Mechanics and Engineering 198(41):3428–3451. https://doi.org/10.1016/j.cma.2009.06.022, URL http://www.sciencedirect.com/science/article/pii/S0045782509002278

Zhang Y, Zhu P, Lai X (2006) Finite element analysis of low-velocity impact damage in composite laminated plates. Materials & design 27(6):513–519